RESIDUAL STRESS SIMULATION OF ALUMINUM CASTINGS USING A TEMPERATURE-DEPENDENT HEAT TRANSFER COEFFICIENT DURING IMMERSION QUENCHING

L. HELML*, S. MAIER**, T. WLANIS*, W. ARTNER***, R. KAHLENBERG*, ****, G. FUCHS*****, E. KOZESCHNIK*

**Institute of Materials Science and Technology, TU Wien, 1060 Vienna, Austria, 0009-0007-3897-6745, lukas.helml@tuwien.ac.at*
***Institute of Production Engineering and Photonic Technologies, TU Wien, 1060 Vienna, Austria, 0009-0006-6489-7699*
****XRC – X-ray center of the TU Wien, TU Wien, 1060 Vienna, Austria*
*****Materials Center Leoben Forschung GmbH, 8700 Leoben, Austria*
******Chair of Metal Forging and Casting, TU Munich, 85748 Garching, Germany*

DOI 10.3217/978-3-99161-089-2-026, license CC BY 4.0

ABSTRACT

A simulation model is developed to predict residual stresses in aluminum castings during immersion quenching. To describe the cooling conditions, a simplified approach is used, in which the heat transfer coefficient is defined as a function of the surface temperature of the component. Two geometries are used in this study: a simple plate to verify the thermal boundary conditions and a stress lattice to evaluate the residual stress distribution. The heat transfer coefficient, which is experimentally validated using the plate geometry, is implemented in a finite element simulation and then applied to the stress lattice. The mechanical behaviour during quenching is characterized using dilatometer experiments. The simulated stress profile in the stress lattice is verified by X-ray diffraction measurements.

Keywords: aluminum casting, heat treatment, residual stress, immersion quenching

INTRODUCTION

In modern production technology, the demand for lightweight components and materials is growing [1,2]. These lightweight components are needed in various applications in the automotive and aerospace industries to further reduce energy consumption and carbon emissions. Several strategies can be used to incorporate lightweight engineering. These include the use of lightweight materials such as aluminum, lightweight construction such as topology-optimized or thin-walled components, and the associated manufacturing process, like forming, casting, welding, heat treatment, and machining.

Traditional manufacturing strategies are often insufficient to meet component requirements such as tolerance and strength. Precise knowledge of the initial residual stresses in these components and the ability to model and simulate them are essential to optimize entire process chains. A concept for a holistic view and optimization of the process chain for the production of aluminum cast components is presented in [3]. Often, the heat treatments have the greatest influence on residual stress-related distortions during machining. There are numerous methods for simulating residual stresses during different heat treatments that describe the material behavior and cooling conditions during quenching with varying degrees of complexity [4].

The heat treatment of aluminum alloys is thoroughly investigated [5-9]. The classical route for aluminum cast parts consists of solution annealing followed by quenching and subsequent ageing to create a T6 temper [5]. The same heat treatment can be applied to aluminum welds as a post-weld treatment. During solution annealing, alloying elements like Mg, Si, and Cu are dissolved in the aluminum lattice. Fast quenching to room temperature then creates a supersaturated solid solution. In the subsequent ageing process, the elements in solid solution form metastable precipitates, which increase the strength of the material through precipitation hardening.

Most of the cast-induced residual stresses are relaxed during the solution heat treatment due to the high annealing temperatures. In contrast, the high temperature gradients during subsequent quenching induce high residual stresses [10-13], which can be partially relaxed during the subsequent ageing treatment [14,15]. Robinson et al. [16] give a good overview of the evolution of residual stresses in heat-treatable aluminum alloys during their heat treatment.

For a reliable simulation of residual stresses during water quenching, an accurate description of the cooling conditions is essential. During immersion quenching of aluminum castings, the heat transfer coefficient α_{imm} passes through three different boiling regimes: film boiling, nucleate boiling, and the convective phase. Initially, when the sample is still at a relatively high temperature, film boiling occurs. During film boiling, the surface of the sample is surrounded by a vapor blanket, resulting in a low α_{imm}. As the part cools and the Leidenfrost temperature is reached, the vapor blanket collapses and the regime transitions to nucleate boiling. The heat transfer coefficient peaks at this stage. When the heat transfer from the sample to the water is no longer sufficient to maintain boiling, the convective stage begins, and α_{imm} decreases accordingly [5]. Maniruzzaman and Sisson [17] observe the same effects and additionally a regime of partial film boiling, resulting in fluctuating surface temperatures due to unstable vapor formation. Xiao et al. [18] use an aluminum test casting to demonstrate the influence of surface orientation relative to the water surface and conclude that α_{imm} is lower for surfaces facing the water surface compared to surfaces in other orientations. The influence

of both the quench medium and sample geometry is documented for wrought and cast aluminum alloys, with corresponding temperature-dependent heat transfer coefficients provided [19-21]. Bamberger et al. [22] investigate the heat transfer coefficients for Al, Cu, and Ni during both spray and immersion quenching with different quenching media, including water and water mixed with organic agents.

The cooling conditions during immersion quenching can also be simulated using computational fluid dynamics (CFD). The immersion quenching process of aluminum castings is studied in this context by [23-27]. CFD enables a more detailed description of all boiling regimes. However, the use of CFD involves a significant additional computational effort and is beyond the scope of this work.

The present work presents an efficient and convenient method for the simulation of residual stresses during water quenching of aluminum castings to improve the process chain. The temperature-dependent mechanical properties of the material are determined experimentally and used to model the material behavior. To model the cooling conditions, a surface temperature-dependent heat transfer coefficient is applied to capture the different boiling regimes during water quenching.

MATERIALS AND EXPERIMENTAL METHODS

GEOMETRIES

In the present work, we focus on two different geometries. The first geometry is a simple plate, which is primarily utilized to determine the heat transfer coefficient during the immersion quenching process. Three type K thermocouples (TCs) are mounted on the plate geometry. TC1 is cast in the center of the body, TC2 and TC3 are fixed on the surface centers. All three TCs are mounted at the same height. The second geometry is a stress lattice, consisting of a thick bar that is connected to a slim bar by two connection bars. The stress lattice is intentionally designed to induce residual stresses. Fig. 1 shows sketches of both geometries and the positioning of the TCs on the plate. The corresponding dimensions are given in Table 1. Stress lattices are often used for stress analysis in cast iron [28-33]. The geometry of stress lattices can vary, but they are usually symmetrical and consist of a thick bar in the center connected to two slim bars on the outside. In contrast, the stress lattice used in this study is asymmetric, similar to a geometry used by Godlewski et al. [15].

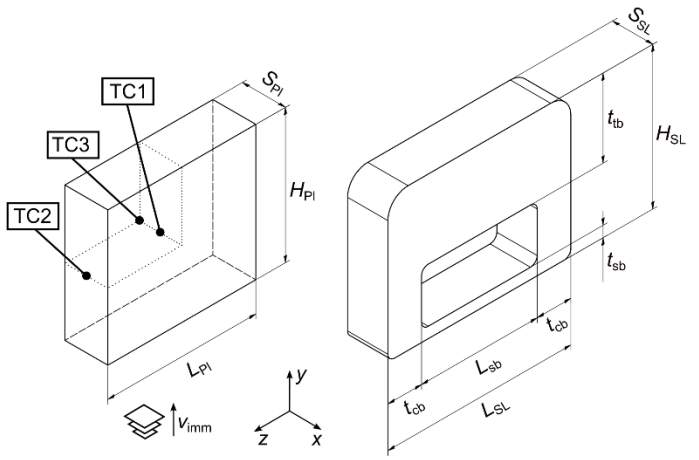

Fig. 1 Sketches of the two geometries used with their main dimensions. On the left is the plate denoted by the subscript 'Pl' with the location of the TCs indicated. On the right is the stress lattice, denoted by the subscript 'SL'. The stress lattice consists of a thick bar (t_{tb}), that is connected to a slim bar (t_{sb}) by two connection bars (t_{cb}).

Table 1 Main dimensions of the plate and stress lattice geometry

Plate:			**Stress Lattice:**		
	L_{Pl}	100 mm		L_{SL}	136 mm
	H_{Pl}	110 mm		H_{SL}	106 mm
	S_{Pl}	30 mm		S_{SL}	30 mm
				L_{sb}	86 mm
				t_{sb}	8 mm
				t_{tb}	58 mm
				t_{cb}	25 mm

MATERIAL

Two different materials are used in this study:

- Plate material: A commercial EN AC-42100 aluminum cast alloy is used for the plate geometry. The plate is produced via gravity casting into a sand mould.
- Stress lattice material: The stress lattice is manufactured from a commercial EN AW-6016 alloy, with an as-cast etching slice provided by AMAG Rolling GmbH. The stress lattice is cut from the slice using a water jet cutter and subsequently milled to its final geometry.

The main chemical composition of both alloys, measured via optical emission spectroscopy (OES), is provided in Table 2.

Due to the high Si content, the cast alloy EN AC-42100 exhibits a microstructure containing eutectic Si. While the eutectic Si influences the mechanical properties of the material, it

remains a challenge to study its isolated effects. To evaluate the matrix behavior independently, we selected a wrought alloy EN AW-6016 in its as-cast state. This alloy has a similar composition to the matrix composition of EN AC-42100 without the eutectic Si. Although the two alloys differ in microstructure and properties [5], they exhibit a comparable precipitation sequence [9], allowing the same traditional heat treatment to be applied. This ensures comparability while eliminating the effects of eutectic Si.

Table 2 Alloy composition of EN AC-42100 and EN AW-6016 measured by OES in wt.%

	Si	Mg	Fe	Cu	Mn	Zn	Ti	Al	other
EN AC-42100	7.42	0.36	0.10	<0.01	0.03	0.02	0.14	91.80	0.13
EN AW-6016	1.07	0.41	0.21	0.07	0.08	<0.01	0.02	98.10	0.04

DETERMINATION OF COOLING CURVES

To determine the temperature history of the plate geometry during water quenching, we use the three mounted TCs. As indicated in Fig. 1**,** the water direction relative to the part is in the positive *y*-direction.

The plate is fixed in a stainless-steel basket and brought up to the solution annealing temperature T_{sol} of 540 °C under ambient atmosphere in a resistance-heated chamber furnace. After reaching an equilibrated temperature at T_{sol} for all three TCs, the basket is removed from the furnace and lowered into a water tank by a winch at a constant immersion velocity v_{imm} of 65 mms^{-1}. This procedure is repeated five times to improve reliability. The initial water temperature T_b is 15 °C. Measuring the water temperature after the quenching process is difficult because the water temperature is not homogeneous throughout the whole water tank. However, Totten and MacKenzie [5] provide a guideline for industrial applications regarding the minimum tank volume for immersion quenching of aluminum. The maximum acceptable temperature increase of the quenchant is 5.5 °C, and based on this limit, the minimum required tank volume is calculated to be 0.027 m^3. For the quench experiments, a tank with a volume of 0.04 m^3 is used, and a water temperature increase of 3.5 °C can be expected. The temperature data is recorded at 10 Hz using a multi-channel recorder.

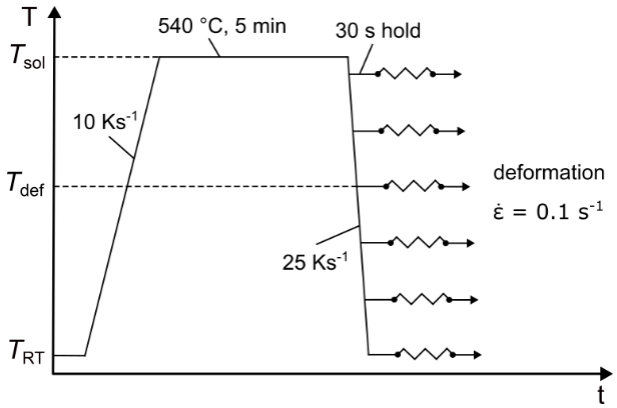

Fig. 2 Thermomechanical treatment in the dilatometer. The pre-solutionized sample is annealed at T_{sol} for 5 min and quenched to T_{def} at 25 Ks^{-1}. After a 30 s isothermal hold, the compression test is carried out isothermally at T_{def}.

The mechanical behavior of the EN AW-6016 alloy during quenching is characterized by compression tests using a Baehr DIL 805 D dilatometer. All samples are pre-solution annealed in batches for 2 hours at T_{sol} and water quenched prior to dilatometer testing. A schematic diagram of the thermomechanical treatment in the dilatometer is shown in Fig. 2. To ensure reproducibility and avoid any effects caused by natural ageing, each sample is again heated to T_{sol} at a rate of 10 Ks^{-1} and shortly solution annealed for 5 min. Using He as the quenching medium, the sample is directly quenched to the deformation temperature T_{def} at a cooling rate of 25 Ks^{-1}. This is followed by an isothermal step at T_{def} for 30 s to ensure thermal stability during the deformation segment.

The isothermal compression test is performed at a strain rate of 0.1 s^{-1} and deformation temperatures ranging from 500 °C to 100 °C in 100 °C increments, plus one test at room temperature (T_{RT} = 22 °C).

RESIDUAL STRESS MEASUREMENTS

The stress measurements are carried out on an Empyrean from Panalytical, equipped with an Eulerian cradle. On the primary side, the beam is filtered with a parallel mirror to separate the Cu $K_{\alpha 1,2}$ radiation, a divergent slit of ½°, a 0.04 rad Soller slit, and a 4 mm mask are used. Detection is made with a parallel plate collimator and a scintillation detector.

For the stress evaluation, the $\sin^2(\psi)$ method is used, which relies on measuring lattice strain variations as a function of the tilt angle ψ. The peaks are measured from 75° to 82° 2θ, and the tilt angle is varied from 0° to 63.43°. By tilting the sample, the diffraction peak shifts and the surface-near biaxial stress state σ_Φ [34]

$$\sigma_{\Phi} = \frac{E_{[hkl]}}{1+\nu}\frac{1}{d_0}\frac{\partial d(\phi,\psi)}{\partial \sin^2(\psi)} \quad (1)$$

can be calculated from the resulting slope in the d-spacing over $\sin^2(\psi)$ plot [35]. For the stress evaluation, we use the (131) Al peak. The Poisson's ratio is 0.33, and the directional Young's Modulus $E_{[hkl]}$ is calculated according to

$$\frac{1}{E_{[hkl]}} = S_{11} - [2(S_{11} - S_{12}) - S_{44}](\alpha^2\beta^2 + \alpha^2\gamma^2 + \beta^2\gamma^2) \quad (2)$$

S_{11}, S_{12}, and S_{44} are the elastic compliances; values are taken from Rösler et al. [34]. α, β, and γ are dependent on the directions [*hkl*]. The resulting directional Young's Modulus in the [131] direction $E_{[131]}$ is 69.61 GPa.

SIMULATION

THERMAL SIMULATION AND THE COOLING CONDITIONS FOR WATER QUENCHING

To simulate the immersion process, we use the commercial finite element (FE) software Ansys 2024 R1. The mesh for the plate geometry consists of 22880 SOLID278 elements with a quadratic element order, resulting in 100271 nodes, and the element shape is HEX8. No symmetry condition is applied to the model.

The first law of thermodynamics postulates the conservation of energy, which is the basis for the heat flow used in transient thermal simulations, taking into account all relevant heat transfer mechanisms to simulate the temperature distribution over time in the part. The thermal boundary condition is a specified heat flux acting on the surface of the part, which significantly influences the thermal history during quenching. This is described by the convective heat flux $\dot{q}$,

$$\dot{q} = \alpha_{\mathrm{imm}}(T_{\mathrm{surf}} - T_{\mathrm{b}}) \quad (3)$$

where α_{imm} is the heat transfer coefficient, T_{surf} is the surface temperature of the part, and T_{b} is the temperature of the quenching medium. Radiative heat transfer is neglected in this proposed model, but can be incorporated into the heat transfer modeling approach described in the following section if desired.

Surface temperature-dependent heat transfer coefficient α_{imm}

To model the heat transfer coefficient α_{imm} during immersion quenching, we follow the approach of Bamberger et al. [22], which proposes that the heat transfer coefficient

$$\alpha_{\mathrm{imm}} = 1.4\sqrt{\lambda\rho C}\exp\left(0.32\frac{T_{\mathrm{surf}}-T_{\mathrm{e}}}{T_{\mathrm{b}}-T_{\mathrm{e}}}\right) + \alpha_{\mathrm{v}} + \alpha_{\mathrm{rad}} \quad (4)$$

depends on the surface temperature of the part T_{surf}, and the temperature-dependent thermophysical material properties of the metal. T_b is the initial bulk water temperature, and T_e is the evaporation temperature of the quench medium. The required material parameters are the thermal conductivity λ, density ρ, and specific heat C.

This concept is valid only for surface temperatures T_{surf} in the range of 900-250 °C. The heat transfer coefficient for stable film evaporation at high surface temperatures α_v is proposed to have a constant value of 750 $Wm^{-2}K^{-1}$, and the heat transfer coefficient for radiation α_{rad} is neglected. For temperatures out of the validity range of Eq. 4 (from 250°C down to room temperature), the heat transfer coefficient is fitted to match the experimentally determined cooling curves.

Implementation of α_{imm} in the FE application

The heat transfer coefficient proposed by Bamberger et al. [22] is dependent on the surface temperature of the specimen, hence it is important for the implementation to use "thermal solid" elements, which allow the film coefficient to be controlled by the surface temperature of the element. Suitable element types include SOLID70, SOLID87, and SOLID278. Note that these types of elements can be used for thermal analysis exclusively.

The initial condition is a homogeneous body temperature of 540 °C, which marks the end of the solution treatment. The immersion process can be divided into three distinct phases. Fig. 3 shows the x-component of the heat flux $\Phi_{q,x}$ and temperature T_s along a surface path s at certain points in time, representing the three phases during the immersion process. During the first phase, all surfaces are exposed to convection against air, with a constant ambient temperature T_{amb} of 25 °C and a convection coefficient α_{amb} of 35 $Wm^{-2}K^{-1}$ applied. This phase corresponds to the removal of the part from the furnace and lowering it into the water tank. The second phase corresponds to the immersion process and begins when the first surface comes into contact with the water. During this phase, two distinct boundary conditions are present. Surface areas that are above the waterline are still subject to convective heat transfer against air. In contrast, surfaces that are already submerged experience convection against water and, therefore, significantly higher heat transfer rates. The surface temperature-dependent heat transfer coefficient α_{imm} is applied to the surface parts that are already submerged. To capture this behavior in the simulation, surface nodes are reselected based on their position relative to the water level. This reselection process corresponds to the immersion velocity v_{imm} used in the experiments. Phase three begins when the part is fully submerged and all surfaces experience convection against the water. α_{imm} is applied to all surfaces during this phase.

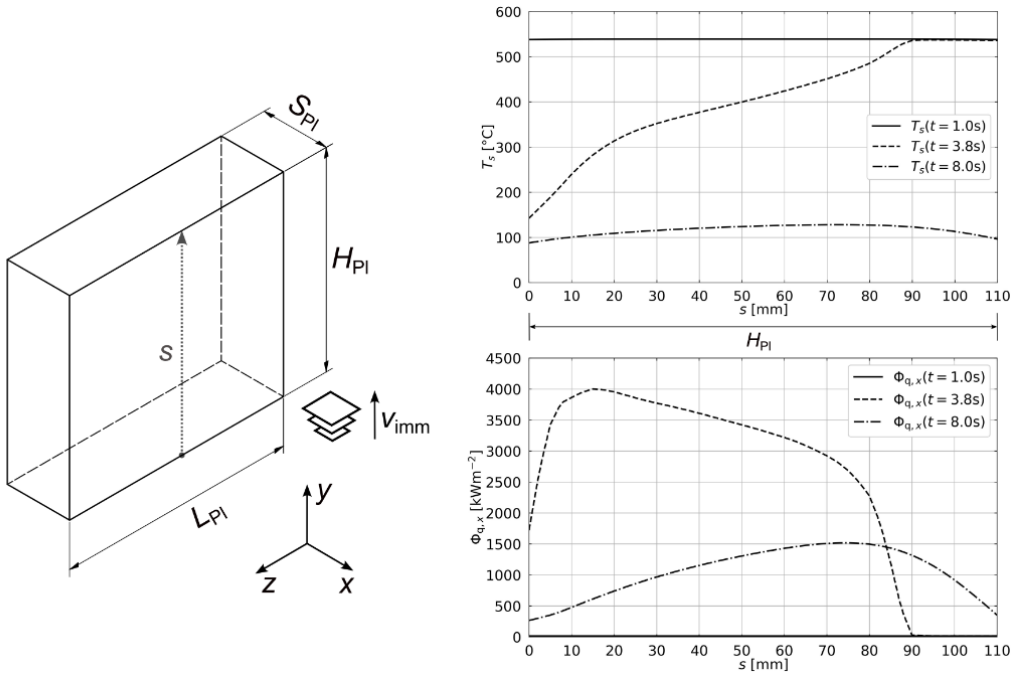

Fig. 3 The sketch on the left shows the plate geometry during immersion quenching. As indicated, the path *s* is located in the middle of the surface of the plate and is oriented in the positive *y*-direction. The plots on the right show simulation results of the temperature profile T_s and the *x*-component of the heat flux $\Phi_{q,x}$ at different points in time over the path *s*. The points in time are chosen to represent the different stages during immersion quenching. After 1 second, the part has not yet come into contact with the water. At 3.8 seconds, the plate is partially submerged, and after 8 seconds, the plate is completely submerged.

This method is applied to the plate geometry, and the results of the thermal analysis are compared to experimental data to determine α_{imm} accordingly, see Fig. 5. The calibrated cooling conditions are then applied to the geometry of the stress lattice. The stress lattice model consists of 101649 SOLID87 elements with quadratic order, resulting in 144896 nodes. The elements have a TET10 shape. No symmetry conditions are applied to the model.

THERMOPHYSICAL PROPERTIES

To describe the temperature distribution of the material during the quenching process, a user-defined material is created in Ansys. The values for the thermophysical properties as a function of temperature, see Fig. 4, are taken from the literature. Overfelt et al. [36] provide specific data for the alloy EN AC-42100 on the density ρ_{mat} and the thermal conductivity κ_{tc}. The isotropic instantaneous coefficient of thermal expansion α_{te} [37] is also specific for the alloy

EN AC-42100. The values for the specific heat at constant pressure c_p [38] refer to pure aluminum.

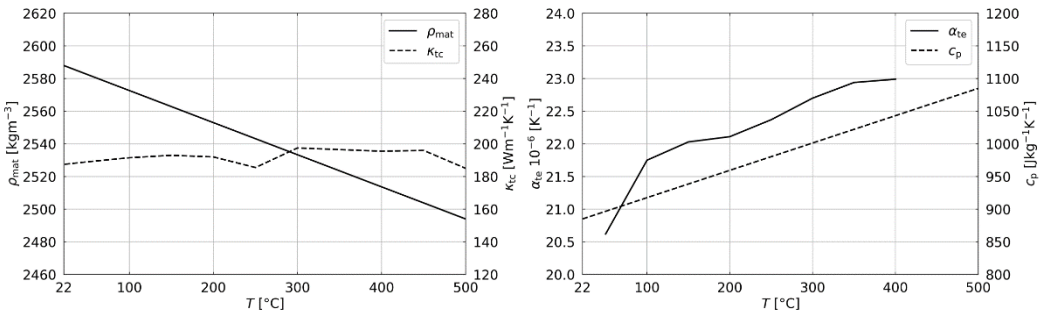

Fig. 4 Thermophysical properties as a function of temperature. The left diagram shows the density ρ_{mat} [36] and the thermal conductivity κ_{tc} [36]. The coefficient of thermal expansion α_{te} [37] and the specific heat at constant pressure c_p [38] are displayed in the right plot.

MECHANICAL SIMULATION

Since the element types used in the thermal simulation are not suitable for structural analysis, and there is no need for a fully thermal-mechanical coupled simulation, the mechanical simulation is performed separately. This is done by applying a unidirectional coupling of the thermal and mechanical analysis. The results of the thermal analysis are used as an imported load in the mechanical model. The temperature history of the part is then mapped onto a mesh that is suitable for structural analysis.

The mechanical simulation is only carried out for the geometry of the stress lattice. The mesh of the mechanical model consists of 40245 SOLID186 elements with quadratic order, resulting in 177395 nodes. No symmetry conditions are applied. As a mechanical boundary condition, the weak springs option is used with a default spring stiffness in the solver controls to prevent rigid body motion. Due to their low stiffness compared to the model stiffness, it can be assumed that they do not have an effect on the stress state during the quenching simulation.

The mapped temperature history is used in the mechanical model to calculate the thermal strain ε_{th} according to

$$\varepsilon_{th} = \alpha_{te}(T)(T - T_{ref}) \tag{5}$$

with the thermal expansion coefficient α_{te} and the reference temperature T_{ref}. Isotropic elasticity via Hooke's law with a temperature-dependent Young's modulus $E(T)$ and a Poisson's ratio ν = 0.33 leads to the description of the elastic strain component ε_{el}. The temperature-dependent Young's Modulus $E(T)$

$$E(T) = (69220\ \text{Pa} - 40.1\ \tfrac{\text{Pa}}{^\circ\text{C}}\ T) \cdot 10^6 \tag{6}$$

is calculated using the default values of MatCalc [39].

The 'Multilinear Isotropic Hardening' model is employed to describe the plastic behaviour. This model assumes isotropic material behaviour and that plasticity is independent of the strain rate. In addition, the Von Mises yield criterion with associative flow rule is applied, which can be described as

$$f(\boldsymbol{\sigma}, \sigma_y) = \overline{\sigma}(\boldsymbol{\sigma}) - \sigma_y \leq 0 \tag{7}$$

with the Von Mises equivalent stress $\bar{\sigma}$ and the yield stress $\sigma_y(T, \varepsilon_{pl})$ according to the temperature-dependent flow curves as measured in the compression tests. The experimentally determined flow curves, see Fig. 7, are discretized and given as tabular data for the hardening model.

RESULTS AND DISCUSSION

TEMPERATURE PROFILES DURING WATER QUENCHING

The calibrated heat transfer coefficient applied to the plate geometry (dashed line) and the calculated values according to Bamberger et al. [22] (solid line) are shown in Fig. 5. In the temperature range (900–250 °C) valid for Eq. 4, α_{imm} closely follows the calculated values. α_{imm} increases steadily with decreasing surface temperature T_{surf} of the part. After reaching a maximum value of 23000 $Wm^{-2}K^{-1}$ at a temperature of 200 °C, α_{imm} decreases significantly. This abrupt decrease of α_{imm} corresponds to the end of the nucleate boiling phase and the transition to the convective stage of cooling.

Fig. 6 shows the simulation results after applying the calibrated heat transfer coefficient (dashed lines) compared to the experimentally determined mean temperatures (solid lines), surrounded by the minimum and maximum values (shaded areas). During the first phase (about 3 seconds), the temperature drops only slightly. This phase corresponds to pure convection against the air when the part has not yet come into contact with the water. Once the part is immersed in the water, the heat flux increases drastically, resulting in rapid cooling to a temperature of about 200 °C. As the heat transfer coefficient decreases at this temperature due to the transition to the convection phase of cooling, the cooling rate also decreases. The simulated initial cooling rate of TC3 is slightly too fast compared to the experiment, but overall, the simulation allows reproduction of the experimentally determined cooling curves of all three TCs with good accuracy.

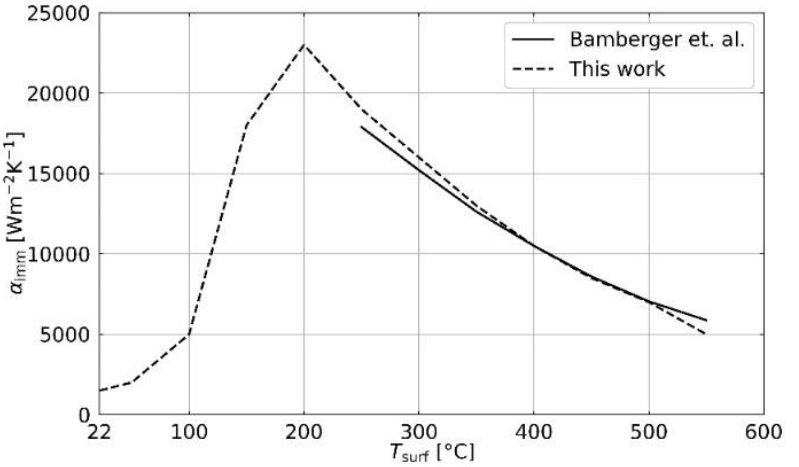

Fig. 5 The heat transfer coefficient used in the present work (dashed line) as a function of the surface temperature of the sample. The theoretical values proposed by Bamberger et al. [22] (solid line) are valid only for temperatures above 250 °C. In the valid range, the applied heat transfer coefficient closely follows the theoretical values. Below a surface temperature of 250 °C, α_{imm} is adjusted accordingly to reproduce the experimental data.

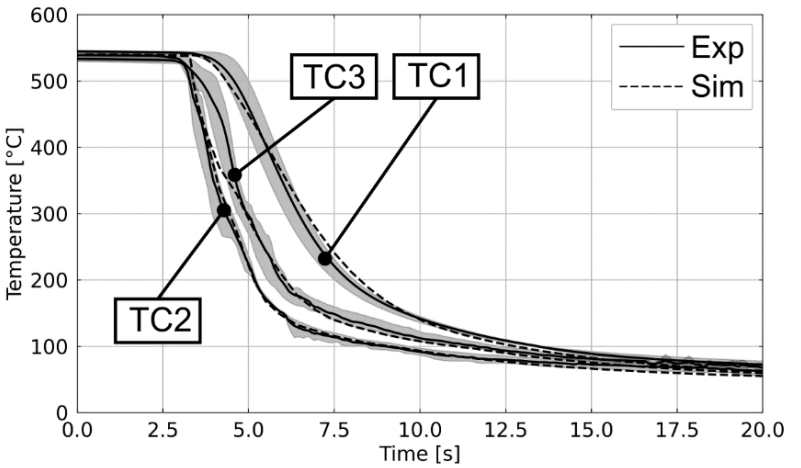

Fig. 6 Temperature curves for all three TCs of the plate geometry after solution annealing and subsequent water quenching. The experiments are repeated five times. Solid lines mark the mean values, enveloped by the shaded areas, representing the minimum and maximum values. The corresponding results of the FE simulation are indicated by dashed lines.

MECHANICAL BEHAVIOUR DURING WATER QUENCHING

The flow curves of the EN AW-6016 alloy from the isothermal compression tests and the corresponding initial yield strength $R_{p0.2}$ as a function of the deformation temperature are shown in Fig. 7. At room temperature, $R_{p0.2}$ is approximately 53 MPa and slightly increases between 100 and 300 °C to a plateau value of approximately 60 MPa. Above 300 °C, the initial yield strength decreases significantly.

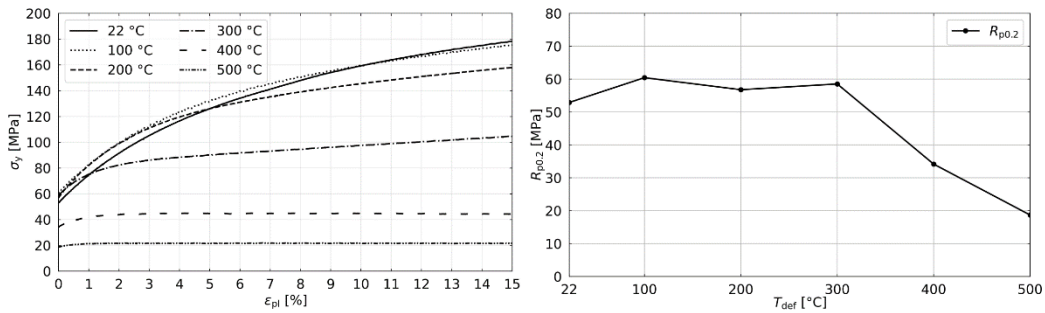

Fig. 7 The left plot shows the experimental data for the yield stress σ_y over true plastic strain ε_{pl} for different deformation temperatures. All flow curves are recorded at a strain rate of 0.1 s^{-1}. On the right, the initial yield strength $R_{p0.2}$ as a function of T_{def} is displayed.

The plateau observed in the $R_{p0.2}$ over T_{def} curve may seem counterintuitive, as the common expressions for the temperature dependency of the yield strength predict a steady decrease with increasing temperature [40]. A possible explanation for this behaviour is the cross-core diffusion effect (CCD) formulated by Curtin et al. [41]. This model describes the contributions of solutes to dynamic strain ageing (DSA) and negative strain rate sensitivity (nSRS), resulting in an increase in the yield strength at elevated temperatures. The underlying mechanism is that solute atoms (e.g., Mg or Si) diffuse to energetically favourable positions within the stress fields around dislocations, thereby hindering dislocation movement. This interaction becomes significant at elevated temperatures, where the diffusivity of the solute atoms is sufficient to enable single-atom jumps through the dislocation core [41]. The effect of CCD on the flow curves is well investigated for Al-Mg alloys [40,42-47]. Since the material in the present work is in a solution-annealed state before quenching, it seems plausible that most Mg and Si atoms are in solid solution and thus contribute to the CCD effect.

In addition to this effect, precipitates can form in the solution-annealed supersaturated condition before and during the compression test, which will also impact the strength of the material. At lower temperatures, this effect will be weak because the time to form the precipitates in larger amounts is insufficient. At medium temperatures, the precipitation strengthening effect under these conditions reaches its maximum effect, until it decreases again at higher temperatures. In the material, both effects will interact with each other and, therefore, lead to a rather complex strengthening behaviour.

The strain rate-dependence is not considered in this analysis, since the flow curves are implemented in tabular form within the multilinear isotropic hardening model. Consequently, the modelled mechanical behaviour is temperature-dependent but not strain rate-dependent. A possible way to take strain rate effects into account in future work is the implementation of the user-defined subroutine 'simple MicroStructure Evolution' (sMSE) [48,49]. sMSE allows for a more detailed material description, including temperature- and strain rate-dependent mechanical properties.

RESIDUAL STRESS AFTER WATER QUENCHING

The simulation results for the residual stress component in the $\varphi = 45°$ direction are shown in Fig. 8. XRD measurements are taken along the surface path $s_{A\text{-}E}$, and compared with the simulation results. The simulation predicts a symmetrical stress profile along this path, with a relatively constant value of $\sigma_{\varphi=45°}$ at -65 MPa, which decreases toward the edges. The measurements show good qualitative agreement with the simulation between the 0 mm and 28 mm marks; however, they deviate somehow beyond this point. Specifically, an asymmetrical stress profile is observed, with a peak value of -103 ± 10 MPa detected at approximately 40 mm. Overall, the simulation consistently underestimates the absolute stress values when compared to the measured data.

The measured peak value of about -100 MPa would imply a plastic strain of approximately 2.5 %, based on the flow curves obtained from compression tests (see Fig. 7). This level of strain appears unrealistic for the quenching process. In contrast, the simulated strain at the same location is about one order of magnitude lower, resulting in a much lower predicted stress value of about -65 MPa.

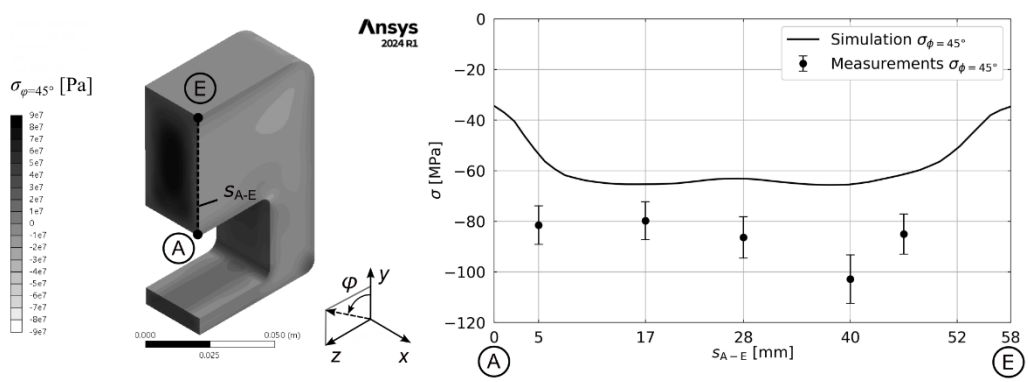

Fig. 8 The Figure shows a cross-section of the stress lattice model with the surface path $s_{A\text{-}E}$ indicated. The simulation results for $\sigma_{\varphi=45°}$ are compared to XRD measurements.

While the simulation captures the general trend of the residual stress distribution along the path $s_{A\text{-}E}$, notable discrepancies remain compared to the XRD measurements. Several factors

may contribute to these discrepancies. One possible explanation is that the calibration of the heat transfer coefficient α_{imm}, based on a simple plate geometry, may not be directly applicable to the more complex stress lattice. To address this issue, further experimental verification is needed. This could be achieved by equipping the stress lattice with thermocouples and comparing simulated cooling curves with data obtained from immersion quenching.

Another potential reason for the discrepancies lies in the limitations of the material description. The hardening model used in the analysis does not account for strain rate-sensitivity, which could affect the accuracy of stress predictions. Furthermore, the thermomechanical treatment applied in the dilatometer for compression tests may not fully represent the material's behaviour under immersion quenching conditions.

SUMMARY

In the present work, we introduce a simulation approach for predicting residual stresses in aluminum cast parts during immersion quenching. A temperature-dependent heat transfer coefficient α_{imm} is developed and implemented in an FE simulation using ANSYS. α_{imm} is experimentally calibrated using a simple plate geometry and subsequently applied to the more complex stress lattice to simulate the generated residual stresses. The mechanical behavior during quenching is experimentally determined using compression tests, and the resulting stress profiles of the stress lattice are validated by XRD measurements.

The following three key statements can be made:

- The applied model accurately reproduces the experimentally determined cooling curves for the plate geometry. The heat transfer coefficient values closely match those reported by Bamberger et al. [22] within their valid temperature range.
- Compression tests show that the initial yield strength $R_{p0.2}$ of EN AW-6016 exhibits a plateau between 100 °C and 300 °C, which might be explained by the effect of CCD. Additionally, precipitation can occur during isothermal holding, resulting in a complex temperature-dependent behavior.
- The simulation predicts a symmetrical residual stress profile along the examined path. In contrast, the XRD measurements show a slightly asymmetrical profile with a local peak. Overall, the absolute values tend to be underestimated by the simulation. While most areas along the surface path show good qualitative agreement between the simulation and measurements, there are still discrepancies that need to be addressed. To enhance the accuracy of the simulation, further refinement of the cooling conditions and the material description is necessary.

ACKNOWLEDGEMENTS

The authors gratefully acknowledge the financial support of the Austrian Research Promotion Agency (FFG) and the German Federal Ministry of Economic Affairs and Energy as part of the Cornet/IGF research program in the research project 369 EN 'Integrated Data-based

Process Chain Optimisation in Casting and Machining – IDaP+' of the FQS-Forschungsgemeinschaft Qualität e. V.

Furthermore, the authors thank AMAG Rolling GmbH for the provision of materials and the X-Ray center (XRC) of the TU Wien for the X-Ray diffraction facilities.

References

[1] CLEARWATER INTERNATIONAL: 'Prognose Zur Materialstruktur in Fahrzeugen Weltweit Im Jahresvergleich 2010 Und 2030', *Statista*, 2016, [Online], Available: https://de.statista.com/statistik/daten/studie/662213/umfrage/prognose-zur-materialstruktur-in-fahrzeugen/. [Accessed: 04-Aug-2025].

[2] CLEARWATER INTERNATIONAL: 'Prognose Zur Menge an Verarbeitetem Aluminium in Fahrzeugkarosserien Weltweit in Den Jahren 2010 Bis 2030', *Statista*, 2016, [Online], Available: https://de.statista.com/statistik/daten/studie/663340/umfrage/prognose-fuer-die-verarbeitete-menge-an-aluminium-in-fahrzeugkarosserien/. [Accessed: 04-Aug-2025].

[3] T. REEBER, M. SICKING, G. FUCHS, S. MAIER, L. HELML, A. KIRNBAUER, H.-C. MÖHRING, D. BIERMANN, W. VOLK, F. BLEICHER and P. H. MAYRHOFER: 'Integrated Data-Based Process Chain in Casting and Machining: A Concept for Holistic Process Improvements', *Production at the Leading Edge of Technology*, W.-G. Drossel, S. Ihlenfeldt, and M. Dix, eds., Springer Nature Switzerland, Cham, pp. 96-103, 2025, https://doi.org/10.1007/978-3-031-86893-1_11.

[4] M. LANDWEHR, F. OEHLER, H. BEHNKEN, H. HOLLING, R. SAMBATHKUMAR, P. GANSER and T. BERGS: 'Influence of Heat Treatment on the Residual Stress-Related Machining Distortion of Ti-6Al-4V Alloy Monolithic Parts', *Procedia CIRP*, 104, pp. 1328-1333, 2021, https://doi.org/10.1016/j.procir.2021.11.223.

[5] G. E. TOTTEN and D. S. MACKENZIE (eds.): *Handbook of Aluminum*, M. Dekker, New York, Basel, 2003.

[6] N. M. SIDDESH KUMAR, DHRUTHI, G. K. PRAMOD, P. SAMRAT and M. SADASHIVA: 'A Critical Review on Heat Treatment of Aluminium Alloys', *Mater. Today Proc.*, 58, pp. 71-79, 2022, https://doi.org/10.1016/j.matpr.2021.12.586.

[7] E. SJÖLANDER and S. SEIFEDDINE: 'The Heat Treatment of Al–Si–Cu–Mg Casting Alloys', *J. Mater. Process. Technol.*, 210(10), pp. 1249-1259, 2010, https://doi.org/10.1016/j.jmatprotec.2010.03.020.

[8] E. SJÖLANDER and S. SEIFEDDINE: 'Artificial Ageing of Al–Si–Cu–Mg Casting Alloys', *Mater. Sci. Eng. A*, 528(24), pp. 7402-7409, 2011, https://doi.org/10.1016/j.msea.2011.06.036.

[9] A. M. A. MOHAMED and F. H. SAMUEL: 'A Review on the Heat Treatment of Al-Si-Cu/Mg Casting Alloys', *Heat Treat. Conv. Nov. Appl.*, p. 55, 2012.

[10] J. S. ROBINSON, S. HOSSAIN, C. E. TRUMAN, A. M. PARADOWSKA, D. J. HUGHES, R. C. WIMPORY and M. E. FOX: 'Residual Stress in 7449 Aluminium Alloy Forgings', *Mater. Sci. Eng. A*, 527(10-11), pp. 2603-2612, 2010, https://doi.org/10.1016/j.msea.2009.12.022.

[11] K. ZHU, B. XIONG, X. LI, Y. ZHANG, Z. LI, Y. LI, K. WEN and L. YAN: 'Finite Element Simulation on Residual Stress during Immersion Quenching and Pre-Stretching of Al7055 Thick Plates', Mater. Res. Express, 9(2), p. 026525, 2022, https://doi.org/10.1088/2053-1591/ac565d.

[12] M. KOÇ, J. CULP and T. ALTAN: 'Prediction of Residual Stresses in Quenched Aluminum Blocks and Their Reduction through Cold Working Processes', *J. Mater. Process. Technol.*, 174(1-3), pp. 342-354, 2006, https://doi.org/10.1016/j.jmatprotec.2006.02.007.

[13] P. JEANMART and J. BOUVAIST: 'Finite Element Calculation and Measurement of Thermal Stresses in Quenched Plates of High- Strength 7075 Aluminium Alloy', *Mater. Sci. Technol.*, 1, p. 765, 1985.

[14] R. WANG, D. RAM, B. STAUDER, R. F. GUTIÉRREZ, E. GARIBOLDI and M. C. POLETTI: 'Stress Relaxation during Artificial Aging of an AlSi7Cu0.5Mg Cast Alloy', *Crystals*, 12(8), p. 1168, 2022, https://doi.org/10.3390/cryst12081168.

[15] L. A. GODLEWSKI, X. SU, T. M. POLLOCK and J. E. ALLISON: 'The Effect of Aging on the Relaxation of Residual Stress in Cast Aluminum', *Metall. Mater. Trans. A*, 44(10), pp. 4809-4818, 2013, https://doi.org/10.1007/s11661-013-1800-1.

[16] J. S. ROBINSON, D. A. TANNER and C. E. TRUMAN: '50th Anniversary Article: The Origin and Management of Residual Stress in Heat-treatable Aluminium Alloys', *Strain*, 50(3), pp. 185-207, 2014. https://doi.org/10.1111/str.12091.

[17] M. MANIRUZZAMAN and R. D. SISSON: 'Heat Transfer Coefficients for Quenching Process Simulation', *J. Phys. IV*, 120, pp. 521-528, 2004, https://doi.org/10.1051/jp4:2004120060.

[18] B. XIAO, Q. WANG, P. JADHAV and K. LI: 'An Experimental Study of Heat Transfer in Aluminum Castings during Water Quenching', *J. Mater. Process. Technol.*, 210(14), pp. 2023-2028, 2010, https://doi.org/10.1016/j.jmatprotec.2010.07.026.

[19] G. S. SARMIENTO, D. M. COSCIA, C. JOUGLARD, G. E. TOTTEN, G. M. WEBSTER, and J. VEGA: 'Residual Stresses, Distortion and Heat Transfer Coefficients of 7075 Aluminum Alloy Probes Quenched in Water and Polyalkylene Glycol Solutions', *ASM Int.*, Materials Park, Ohio, pp. 1118-1124, 2000.

[20] Y. N. LI, Y. A. ZHANG, X. W. LI, Z. H. LI, G. J. WANG, H. W. YAN, L. B. JIN and B. Q. XIONG: 'Effects of Heat Transfer Coefficients on Quenching Residual Stresses in 7055 Aluminum Alloy', Mater. Sci. Forum, 877, pp. 647-654, 2016, https://doi.org/10.4028/www.scientific.net/msf.877.647.

[21] X. YANG, J. ZHU, Z. LAI, Y. LIU, D. HE and Z. NONG: 'Finite Element Analysis of Quenching Temperature Field, Residual Stress and Distortion in A357 Aluminum Alloy Large Complicated Thin-Wall Workpieces', *Trans. Nonferrous Met. Soc. China*, 23(6), pp. 1751-1760, 2013, https://doi.org/10.1016/s1003-6326(13)62657-6.

[22] M. BAMBERGER and B. PRINZ: 'Determination of Heat Transfer Coefficients during Water Cooling of Metals', *Mater. Sci. Technol.*, 2(4), pp. 410-415, 1986, https://doi.org/10.1179/mst.1986.2.4.410.

[23] D. GREIF, R. KOPUN, N. KOSIR and D. ZHANG: 'Numerical Simulation Approach for Immersion Quenching of Aluminum and Steel Components', *Int. J. Automot. Eng.*, 8(2), pp. 45-49, 2017, https://doi.org/10.20485/jsaeijae.8.2_45.

[24] R. KOPUN, L. ŠKERGET, M. HRIBERŠEK, D. ZHANG, B. STAUDER and D. GREIF: 'Numerical Simulation of Immersion Quenching Process for Cast Aluminium Part at Different Pool Temperatures', *Appl. Therm. Eng.*, 65(1-2), pp. 74-84, 2014, https://doi.org/10.1016/j.applthermaleng.2013.12.058.

[25] V. SRINIVASAN, K.-M. MOON, D. GREIF, D. M. WANG and M. KIM: 'Numerical Simulation of Immersion Quench Cooling Process Using an Eulerian Multi-Fluid Approach', *Appl. Therm. Eng.*, 30(5), pp. 499–509, 2010, https://doi.org/10.1016/j.applthermaleng.2009.10.012.

[26] V. SRINIVASAN, K. MOON, D. GREIF, D. WANG and M. KIM: 'Numerical Simulation of Immersion Quench Cooling Process: Part I', *Volume 10: Heat Transfer, Fluid Flows, and Thermal Systems, Parts A, B, and C*, ASMEDC, Boston, Massachusetts, USA, pp. 1941-1954, 2008, https://doi.org/10.1115/imece2008-69280.

[27] V. SRINIVASAN, K.-M. MOON, D. GREIF, D. M. WANG and M. KIM: 'Numerical Simulation of Immersion Quenching Process of an Engine Cylinder Head', *Appl. Math. Model.*, 34(8), pp. 2111-2128, 2010, https://doi.org/10.1016/j.apm.2009.10.023.

[28] U. QUACK, W. STETS and G. WOLF: 'Messung Und Simulation von Eigenspannungen in Gusseisen', *Giesserei*, 97(11), p. 50, 2010.

[29] Y. MOTOYAMA, H. TAKAHASHI, T. OKANE, Y. FUKUDA and M. YOSHIDA: 'Numerical and Experimental Study on Residual Stress in Gray Cast Iron Stress Lattice Shape Casting', *Metall. Mater. Trans. A*, 44(7), pp. 3261-3270, 2013, https://doi.org/10.1007/s11661-013-1683-1.

[30] Y. MOTOYAMA, D. INUKAI, T. OKANE and M. YOSHIDA: 'Verification of the Simulated Residual Stress in the Cross Section of Gray Cast Iron Stress Lattice Shape Casting via Thermal Stress Analysis', *Metall. Mater. Trans. A*, 45(4), pp. 2315-2325, 2014, https://doi.org/10.1007/s11661-013-2126-8.

[31] E. M. JOHNSON, T. R. WATKINS, J. E. SCHMIDLIN and S. A. DUTLER: 'A Benchmark Study on Casting Residual Stress', *Metall. Mater. Trans. A*, 43(5), pp. 1487-1496, 2012, https://doi.org/10.1007/s11661-011-0907-5.

[32] P. HOFER, E. KASCHNITZ and P. SCHUMACHER: 'Distortion and Residual Stress in High-Pressure Die Castings: Simulation and Measurements', *JOM*, 66(9), pp. 1638-1646, 2014, https://doi.org/10.1007/s11837-014-1118-5.

[33] E. GUSTAFSSON, M. HOFWING and N. STRÖMBERG: 'Residual Stresses in a Stress Lattice–Experiments and Finite Element Simulations', *J. Mater. Process. Technol.*, 209(9), pp. 4320-4328, 2009, https://doi.org/10.1016/j.jmatprotec.2008.11.025.

[34] J. RÖSLER, H. HARDERS and M. BÄKER: *Mechanisches Verhalten der Werkstoffe*, Springer Fachmedien Wiesbaden, Wiesbaden, 2019, https://doi.org/10.1007/978-3-658-26802-2.

[35] L. SPIEß, G. TEICHERT, R. SCHWARZER, H. BEHNKEN and C. GENZEL: *Moderne Röntgenbeugung: Röntgendiffraktometrie für Materialwissenschaftler, Physiker und Chemiker*, Springer Fachmedien Wiesbaden, Wiesbaden, 2019, https://doi.org/10.1007/978-3-8348-8232-5.

[36] R. OVERFELT, S. BAKHTIYAROV and R. TAYLOR: 'Thermophysical Properties of A201, A319, and A356 Aluminium Casting Alloys', *High Temp.-High Press.*, 34(4), pp. 401-409, 2002, https://doi.org/10.1068/htjr052.

[37] M. B. GRIEB, H.-J. CHRIST and B. PLEGE: 'Thermomechanical Fatigue of Cast Aluminium Alloys for Cylinder Head Applications–Experimental Characterization and Life Prediction', *Procedia Eng.*, 2(1), pp. 1767-1776, 2010, https://doi.org/10.1016/j.proeng.2010.03.190.

[38] E. H. BUYCO and F. E. DAVIS: 'Specific Heat of Aluminum from Zero to Its Melting Temperature and beyond. Equation for Representation of the Specific Heat of Solids', *J. Chem. Eng. Data*, 15(4), pp. 518-523, 1970, https://doi.org/10.1021/je60047a035.

[39] E. KOZESCHNIK: 'Mean-Field Microstructure Kinetics Modeling', *Encyclopedia of Materials: Metals and Alloys*, Elsevier, pp. 521-526, 2022, https://doi.org/10.1016/B978-0-12-819726-4.00055-7.

[40] J. KREYCA and E. KOZESCHNIK: 'State Parameter-Based Constitutive Modelling of Stress Strain Curves in Al-Mg Solid Solutions', *Int. J. Plast.*, 103, pp. 67-80, 2018, https://doi.org/10.1016/j.ijplas.2018.01.001.

[41] W. A. CURTIN, D. L. OLMSTED and L. G. HECTOR: 'A Predictive Mechanism for Dynamic Strain Ageing in Aluminium–Magnesium Alloys', *Nat. Mater.*, 5(11), pp. 875-880, 2006, https://doi.org/10.1038/nmat1765.

[42] B. VIERNSTEIN, P. SCHUMACHER, B. MILKEREIT and E. KOZESCHNIK: 'State Parameter-Based Simulation of Temperature- and Strain Rate Dependent Flow Curves of Al-Alloys', *Light Met.*, pp. 267-271, 2020, https://doi.org/10.1007/978-3-030-36408-3_38.

[43] P. SCHUMACHER: *Plastisches Verformungsverhalten unterkühlter Aluminiumlegierungen im System Al-Mg-Si*, Dissertation, Universität Rostock, 2018.

[44] F. KABIRIAN, A. S. KHAN and A. PANDEY: 'Negative to Positive Strain Rate Sensitivity in 5xxx Series Aluminum Alloys: Experiment and Constitutive Modeling', *Int. J. Plast.*, 55, pp. 232-246, 2014, https://doi.org/10.1016/j.ijplas.2013.11.001.

[45] R. C. PICU, G. VINCZE, F. OZTURK, J. J. GRACIO, F. BARLAT and A. M. MANIATTY: 'Strain Rate Sensitivity of the Commercial Aluminum Alloy AA5182-O', *Mater. Sci. Eng. A*, 390(1-2), pp. 334-343, 2005, https://doi.org/10.1016/j.msea.2004.08.029.

[46] S. SAMANTA, J. R. SAHOO and S. MISHRA: 'Effect of Dynamic Strain Ageing on Flow Stress and Critical Strain for Jerky Flow in Al-Mg Alloys', *Int. J. Plast.*, 180, p. 104053, 2024, https://doi.org/10.1016/j.ijplas.2024.104053.

[47] S. L. YAN, H. YANG, H. W. LI and X. YAO: 'Variation of Strain Rate Sensitivity of an Aluminum Alloy in a Wide Strain Rate Range: Mechanism Analysis and Modeling', *J. Alloys Compd.*, 688, pp. 776-786, 2016, https://doi.org/10.1016/j.jallcom.2016.07.077.

[48] B. VIERNSTEIN, T. WOJCIK and E. KOZESCHNIK: 'State Parameter-Based Yield Strength Model for Integration in Finite Element User-Material Routines', *Metals*, 12(7), p. 1207, 2022, https://doi.org/10.3390/met12071207.

[49] Y. V. SHAN, B. VIERNSTEIN and E. KOZESCHNIK: 'Microstructure Evolution Subroutine for Finite Element Analysis', Math. Model. Weld Phenom., 13, pp. 407-412, 2023, https://doi.org/10.3217/978-3-85125-968-1-22.